



Final Draft **of the original manuscript**

Chen, L.; Blawert, C.; Yang, J.; Hou, R.; Wang, X.; Zheludkevich, M.;
Lia, W.:

**The stress corrosion cracking behaviour of biomedical Mg-1Zn
alloy in synthetic or natural biological media.**

In: Corrosion Science. Vol. 175 (2020) 108876.

First published online by Elsevier: 18.07.2020

<https://dx.doi.org/10.1016/j.corsci.2020.108876>

The stress corrosion cracking behaviour of biomedical Mg-1Zn alloy in synthetic or natural biological media

Lianxi Chen^{a, b, c}, Carsten Blawert^c, Junjie Yang^a, Ruiqing Hou^a, Xiaojian Wang^{a*},

Mikhail L. Zheludkevich^c and Wei Li^{a, b*}

^a Institute of Advanced Wear & Corrosion Resistant and Functional Materials, Jinan University,
Guangzhou, 510632, China;

^b National Joint Engineering Center of High-performance Wear-resistant Metallic Materials,
Guangzhou, 510632, China;

^c Magnesium Innovation Centre (MagIC), Institute of Materials Research, Helmholtz-Zentrum
Geesthacht, Geesthacht, 21502, Germany

* E-mail addresses: xiaojian.wang@jnu.edu.cn (X Wang), liweijnu@126.com (W Li)

Abstract □

In the present study, the effects of degradation environment on the *in vitro* stress corrosion cracking (SCC) behaviour of biomedical Mg-1Zn alloy were investigated. The resistance to SCC's initiation and propagation for Mg-1Zn alloy in synthetic cell culture medium and natural bovine calf serum (BCS) were improved compared to phosphate-buffered saline (PBS) and modified simulated body fluid (m-SBF), due to the homogenous corrosion and spontaneous adsorption of organic components. The elongation to failure obtained in BCS was reduced by around 30 % compared with that of the sample tested in air, indicating still a good ductility for Mg alloy.

Keywords: A. Magnesium; B. XPS; C. Hydrogen embrittlement; C. Stress corrosion

1 Introduction

Mg and its alloys have attracted increasing attention as biodegradable metallic materials in the past decades [1,2]. Comparing to bio-polymers and bio-ceramics, Mg alloys have a good combination of toughness and mechanical strength [3]. Mg alloys possess similar physical and mechanical properties than bone, thus can effectively weakening the “stress shielding effect”. Meanwhile, the degradability of implant materials can avoid second surgery after the tissue healing [4].

Mg alloys can suffer from plastic deformation during the implant deployment, and biomechanical after fixation in the body. For instance, the bone plate sustains a certain tensile stress and bend loading during service and normal walking [5]. The cardiovascular stent experiences huge deformation during the interventional operation and cyclic loading of the cardiac impulse [6]. Synergistic effects of mechanical loading and corrosive physiological solution can cause an unstable shape and surface morphology for the bulk materials, even resulting into a corrosion-assisted cracking failure, for instance stress corrosion cracking (SCC) [7,8]. Prabhu et al. [9] found that the ultimate tensile strength (UTS) and elongation to failure (ϵ) of Mg-4Zn alloys decreased by 58 % and 80 % respectively, when slow strain rate tensile (SSRT) tests were performed in simulated physiological fluid. If the SCC fracture occurs, it would result in premature implant failure, troublesome removal operation, even inflammation of the surrounding tissues, and so on [10]. Therefore, investigating the influence of biomechanical or strain on the degradation behaviour of biomedical Mg alloys is essential for the evaluation of the service period of biodegradable implants.

In general, the stress corrosion cracking (SCC) of Mg alloy is critically influenced by the alloy microstructure and the service environment to which it is exposed [11]. SCC is generally related to two main mechanisms: anodic dissolution (AD) or hydrogen-assisted cracking processes (hydrogen

embrittlement, HE) [7,12]. AD can be solely related to intergranular stress corrosion cracking (IGSCC), which was induced by the accelerated corrosion of Mg matrix along grain boundaries due to precipitated second phases [13,14]. The second phases can be removed by heat treatment thus avoiding the possibility of IGSCC [15]. Besides, AD failed to explain some fluted transgranular facets which often observed on the fracture surfaces of Mg alloys caused by transgranular SCC (TGSCC) [9,16,17]. Hence, some literatures suggest that such observations with regard to TGSCC in Mg triggered by HE. Cao et al. [18] and Shi et al. [15] found that distilled water (DW) was sufficient to cause the TGSCC of Mg alloys. It is believed that hydrogen evolving during dissolution of the base metal could be absorbed by Mg matrix, thus promoting the hydrogen assisted cracking [16,19].

Human body fluid contains metal ions (calcium, magnesium etc.), phosphates and carbonates, as well as aggressive chloride ions (Cl^-) [20,21]. The formation and deposition of magnesium hydroxide and hydroxyapatite-based compounds on the surface could provide a certain protection for Mg alloys [21,22]. However, Cl^- can induce localized breakdown or dissolution of the passive film, thereby leading to pitting corrosion [7]. Pits are also essential for aqueous-assisted cracking of Mg alloys because they provide stress concentration sites, through which atomic hydrogen can penetrate and cause embrittlement or early cracking of the materials [23,24]. Except for ions such as chlorides, human blood plasma contains essential organic components such as amino acids, glucose and proteins, which play an important role in the degradability of Mg alloys. These organic components can be spontaneously adsorbed on the surface of implants [25,26], which is achieved by Van Der Waals, electrostatic interactions and hydrophobic, as well as hydrogen bonding [27]. Wagener et al. [28] observed an increased corrosion resistance for Mg alloy owing to bovine serum albumin-containing physical shield layer formed on the surface during the initial stages of immersion tests. Wang et al. [25]

found that a deformed metallic surface could improve the electrostatic force, facilitating the adsorption of the negatively charged albumin onto the alloy surface. On the other hand, proteins chelating with metal ions also form colloidal organometallic complexes, whose migration from the surface results in the increasing dissolution of Mg alloys [27,29]. Therefore, it is critical to consider the effect of adsorption or chelation induced by the organic components on the SCC behaviour of Mg alloys, i.e., to provide protection or deterioration.

Simulated body solutions with different buffering system were used to investigate the *in vitro* degradation behaviour of Mg alloys: phosphate-buffered saline (PBS) [30], modified simulated body fluid (m-SBF) and cell culture medium (Dulbecco's modified eagle medium (DMEM)) [21]. Different simulated solutions lead to different corrosion rates and degradation products, indicating various corrosion pathways of Mg [31]. Synthetic solutions containing inorganic salts similar to plasma (*e.g.* m-SBF and simulated body fluid (SBF)) have been used to investigate the SCC behaviour of Mg alloys [14,32,33]. However, the organic-containing media, such as DMEM and natural derived media (*i.e.* bovine calf serum (BCS)) were rarely used for the SCC studies of biomedical Mg alloys. At the same time, *in vitro* stress corrosion cracking tests are imperative to screen suitable candidates for bio-Mg alloys. Therefore, it is of importance to measure the SCC susceptibility of Mg alloys in suitable simulated body fluid solutions.

The object of this work is to study the *in vitro* degradation and stress corrosion cracking behaviour of Mg alloy in synthetic and natural biological media. To avoid the negative influence of the microstructure and second phases of Mg alloys on SCC, a low alloyed and extruded Mg-1Zn alloy was selected. The following simulated physiological media were used in this work: PBS, m-SBF, DMEM and BCS, and compared with distilled water (DW) and air were applicable. Electrochemical analysis,

immersion testing and slow strain rate tensile (SSRT) testing in combination with electrochemical monitoring were conducted to understand the mechanism involved in SCC susceptibility of Mg-1Zn alloy.

2 Experimental

2.1 Materials and media

The magnesium (Mg) alloy selected in the present study was a wrought Mg-1Zn alloy. The chemical composition of this alloy is following: 1.24 wt% Zn, 0.0031 wt% Cu, 0.051 wt% Al, 0.0012 wt% Ni, 0.0063 wt% Fe, 0.034 wt% Mn and magnesium balanced. Bulk samples of $2 \times 10 \times 10 \text{ mm}^3$ were prepared. These samples were wet ground with 600# to 2500# SiC paper, and ultrasonically washed in anhydrous alcohol and sterilized with acetone for 10 min, then characterized using scanning electron microscope (SEM; Phenom XL) with energy-dispersive spectroscopy (EDS) at 15 kV of acceleration voltage. For optical microscopy (OM; Leica, DM3000) observation, ground samples were etched with 3 % nitric acid and a picric acid-based etchant, which consisted out of 70 mL ethanol, 10 mL acetic acid, 5 g picric acid and 20 mL distilled water (DW).

The four types of physiological solutions used in this work and their compositions are shown in Table 1. Buffered modified simulated body fluid (m-SBF) was prepared according to previous report [34]. Distilled water (DW) was employed to study the intrinsic stress corrosion cracking susceptibility of Mg alloy in aqueous solution. Bovine calf serum (BCS, MP20005, Shanghai Yuanye Bio-Technology Co., Ltd), containing various hormones, plasma proteins, fats, polypeptides, growth factors, carbohydrates, inorganic salts, etc. was selected as natural biological solution. PBS and DMEM were purchased from Thermo Fisher Scientific USA. All media were prepared in an aseptic condition and sterilized by autoclaving or filtration.

Table 1 Chemical composition of the simulated physiological media.

Ingredient	Plasma	PBS	m-SBF	DMEM	BCS
Na ⁺ (mmol·L ⁻¹)	142	157	142	155.3	
K ⁺ (mmol·L ⁻¹)	5.0	4.1	5.0	5.3	
Ca ²⁺ (mmol·L ⁻¹)	2.5	-	3.75	1.8	
Mg ²⁺ (mmol·L ⁻¹)	1.5	-	1.5	0.8	
Cl ⁻ (mmol·L ⁻¹)	103	140	148.8	115.7	Bovine Calf
HCO ₃ ⁻ (mmol·L ⁻¹)	27.0	-	4.2	44.1	Serum (BCS)
HPO ₄ ²⁻ (mmol·L ⁻¹)	1.0	11.5	1.5	0.9	is an
H ₂ PO ₄ ⁻ (mmol·L ⁻¹)	-	2.06	-	-	animal-derived
SO ₄ ²⁻ (mmol·L ⁻¹)	0.5	-	0.5	0.8	product
Amino acids (mmol·L ⁻¹)	Variable	-	-	10.6	without
Dex/glucose (mmol·L ⁻¹)	3.6-5.2	-	-	4.5	chemical
Vitamins (mmol·L ⁻¹)	-	-	-	0.15	additives
Phenol red (g·L ⁻¹)	-	-	-	0.04	
HEPES (mmol·L ⁻¹)	-	-	75	-	
Proteins	63-80	-	-	-	
Reference	[20,21]	[35]	[36]	[35]	

2.2 Hydrogen evolution and electrochemical tests

The evolved hydrogen volume during immersion tests were determined in DW, PBS, m-SBF, DMEM and BCS at 37 ± 1 °C under sterilized conditions, as described in our previous work in detail [37]. Three duplicates were prepared for each solution for immersion tests. The ratio of the exposed surface area (cm²) to the solution volume (mL) was kept at 1:40. In order to simulate the body fluid exchange in physiological environments, 50 % of the testing solution was refreshed every 48 h. The hydrogen evolution rate (HER, mL·cm⁻²·h⁻¹) was denoted as:

$$\text{HER} = \frac{v}{st} \quad (1)$$

Where v refers to H₂ gas volume (mL), s refers to the specimen area (cm²), and t refers to the immersion testing time (h). The surface morphologies and composition after the immersion tests were observed using SEM and EDS, subsequently the corrosion products were removed in chromic acid (200

g·l⁻¹ chromium (VI) oxide and 10 g·l⁻¹ AgNO₃ in distilled water) for 20 min immersion at room temperature. In order to provide three-dimensional information of the surface of the corrosion products-removed samples, a topographical mode of Phenom XL, in which the signals are subtracted as the quadrant backscattered electron detector divided into two opposite groups, was used.

Potentiodynamic polarization (PDP) and electrochemical impedance spectroscopy (EIS) of Mg alloy in different media at 37 ± 1 °C were measured using an electrochemical workstation (PARSTAT4000, USA). A conventional three-electrode system was used, where the samples served as the working electrode (1 cm²), a platinum sheet as the counter electrode and a saturated calomel electrode (SCE) as the reference electrode. Due to the low conductivity, distilled water (DW) was not used in all the electrochemical tests. Before the PDP or EIS measurement, samples were placed in the testing media for 30-60 min to reach the stable open circuit potential (OCP). The PDP was performed from -250 mV to +250 mV with respect to the OCP, at a scanning rate of 0.5 mV·s⁻¹. The impedance measurement was taken from 1×10^5 to 1×10^{-1} Hz with 10 mV peak to zero amplitude vs. OCP with X points per frequency decade. Three duplicate specimens were measured to guarantee the reproducibility of the data. The corrosion potential (E_{corr}) and corrosion current density (i_{corr}) were derived by Origin8.0 software from the PDP slopes. Due to the anodic branch of polarization curve of Mg is unfortunately not following the activation control kinetics, the corrosion current calculation was measured by the cathodic branches that commenced about 50 mV from corrosion potential. Its use for estimation of the corrosion current density is justifiable and often reported in the literatures on Mg corrosion [38-40].

2.3 Corrosion products characterization

The chemical composition and structure of the surface layer of the Mg alloy were characterized by Fourier transform infrared spectra (FTIR, Nicolet iS50, Thermo Fisher Scientific) and X-ray photoelectron spectroscopy (XPS, ESCALAB 250Xi, Thermo Fisher Scientific) after 48 h immersion in different solutions. XPS was employed with Al K α source (1486.6 eV), and its binding energies were calculated with regard to carbon (C 1s) at 284.8eV. Phase of Mg-1Zn alloy was characterized by X-ray diffraction (XRD, D/Max-2400, Japan) with monochromatic Cu-K α radiation, at a scan rate of 4 °·min⁻¹ and a step size of 0.02 ° within 2 θ = 20-90 °.

2.4 Slow strain rate tensile tests combined with electrochemical tests

The stress-assisted degradation of the Mg-1Zn alloy in different media was studied using a slow strain rate tensile (SSRT) device combined with electrochemical workstation, according to our previous work [41]. Dumbbell-shaped round tensile samples with 3 mm (diameter) and gauge dimension of 16 mm (length) were tested at a strain rate of $1 \times 10^{-6} \text{ s}^{-1}$. The strain rate used in the tests was enough to perform the stress corrosion cracking of Mg alloy according to the standard (ISO 7539-7:2005) [42]. Then, the testing time might be in a suitable range to avoid certain negative factors, such as high risk of contamination in an open environment during long-term testing [43]. During the slow tensile tests, the open circuit potential (OCP) of the SSRT samples was recorded. Three duplicate specimens were measured to guarantee the reproducibility of the data. The ultimate tensile strength (UTS), yield strength (YS) and elongation to failure (ϵ) was derived from the engineering stress-strain plots. The reduction in area (R_A) was calculated using [18]:

$$R_A = \frac{A_0 - A_f}{A_0} \times 100\% \quad (2)$$

Where A_0 (mm²) represents the original sample sectional area, and A_f (mm²) is the measured

minimum sectional area after the SSRT tests.

The stress corrosion cracking (SCC) susceptibility index (I_{SCC}) of the Mg-1Zn alloy were calculated using the ultimate tensile strength (UTS) or elongation to failure (ϵ) based on that of samples tested in air and in different media. The I_{SCC} was denoted as [12]:

$$I_{SCC} = \frac{(\text{UTS or } \epsilon)_{in\ air} - (\text{UTS or } \epsilon)_{in\ media}}{(\text{UTS or } \epsilon)_{in\ air}} \quad (3)$$

A value of I_{SCC} close to zero indicates that Mg alloy is immune to SCC; on the contrary, a high value suggests a greater SCC susceptibility. After the SSRT tests, samples were cleaned with distilled water. After drying, their fracture morphologies and corrosion products were measured using SEM and EDS.

3 Results

3.1 Microstructure of the samples

In order to study the microstructure of the extruded Mg-1Zn alloy, ground and etched samples were observed using SEM, and optical microscopy (OM), as shown in Fig. 1. Optical metallographic image (left in Fig. 1a) shows that the grain size was 5~30 μm . Except the matrix phase of $\alpha\text{-Mg}$, secondary phase (MgZn) could hardly be found and detected in the SEM images and XRD analysis (Fig. 1b).

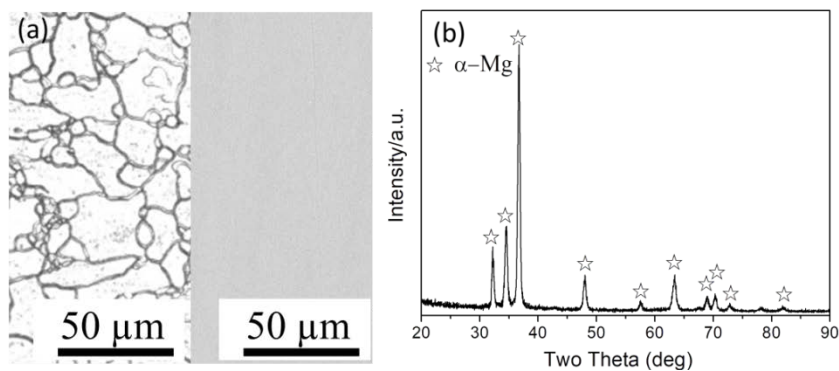


Fig. 1 The (a) optical metallographic micro-graph (left, etched sample) and SEM (right, ground sample) in backscattered electron mode; (b) XRD analysis of the Mg-1Zn alloy

3.2 Immersion and electrochemical tests

Fig. 2 shows the hydrogen evolution tests of the Mg-1Zn alloy immersed in different aqueous solutions at 37 ± 1 °C for 48 h. The data shows that the total volume of hydrogen gas of the samples (inset in Fig. 2) immersed in different solutions follows this order: m-SBF > BCS > DMEM > PBS > DW. The corrosion rate based on the hydrogen evolution rate indicates that the highest and the lowest corrosion rate were found in m-SBF and DW, respectively. During the initial stage of immersion tests, the hydrogen evolution rate of samples tested in m-SBF was significantly higher than in the other solutions. However, all of the samples tested in PBS, DMEM and BCS showed a slow increase of hydrogen gas volume as a function of immersion time. The difference in hydrogen evolution of the Mg alloy is significantly related to the composition of the physiological media.

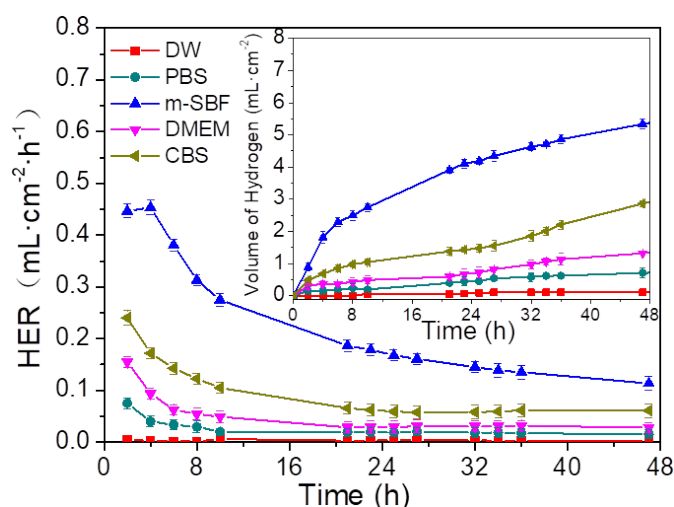


Fig. 2 Hydrogen evolution of Mg-1Zn alloy in DW, PBS, m-SBF, DMEM and BCS as a function of immersion time at 37 ± 1 °C; hydrogen evolution rate (HER).

The potentiodynamic polarization (PDP) and the electrochemical impedance spectroscopy (EIS) tests of the Mg-1Zn alloy measured in PBS, m-SBF, DMEM and BCS after 0.5 h of immersion at 37 ± 1 °C are shown in Fig. 3. Fig. 3a shows the PDP plots. Fig. 3b, c and d shows the Nyquist, Bode plots and the fitting curves. The highest frequencies in Bode plots are probably affected by the experimental

artifact (pseudo-inductive behaviour). The corrosion potential (E_{corr}) and corrosion current density (i_{corr}) obtained from these potentiodynamic polarization plots as well as the fitted impedance results according to the spectra data and the equivalent circuit (Fig. 3c) are listed in Table 2. The surface film on the Mg alloy was related to the gradually deposition or adsorption of inorganic or organic components as a function of testing time [44]. The equivalent circuit model in Fig. 3c is physically interpreted as follows: R_s is the solution resistance, R_l and CPE_l are introduced to account for the surface passive film. R_{ct} represents the charge transfer resistance parallel to the capacity depicted by a constant phase element (CPE_{dl}) [45]. CPE_{dl} refers to the electric double layer capacity at the interface of the Mg alloy and electrolyte. The CPE is usually applied to describe a non-ideal capacitive behaviour, and is defined by two factors, n and Y_0 . If n is equal to 1, CPE is identical to a capacitor. When $n = 0$, CPE is a resistor yield and $n = -1$ is an inductor yield [46].

It can be seen from Fig. 3a and Table 2 that E_{corr} obtained from samples tested in PBS, m-SBF, DMEM and BCS is -1.53, -1.67, -1.65 and -1.63 V, respectively. The corrosion current density i_{corr} is 4, 267, 11 and 12 $\mu\text{A}\cdot\text{cm}^{-2}$, correspondingly. The value of R_l for the samples tested in PBS, m-SBF, DMEM and BCS is 3319, 118, 926.4 and 999.8 $\Omega\cdot\text{cm}^2$, respectively. R_{ct} is 845, 85, 539 and 544 $\Omega\cdot\text{cm}^2$, correspondingly. The corrosion current i_{corr} obtained from in m-SBF is about two order of magnitude higher than that in PBS, and the value of R_l and R_{ct} obtained in m-SBF is about two order of magnitude lower than that in PBS. The value of E_{corr} , i_{corr} , R_l and R_{ct} measured in DMEM and BCS is almost similar. These results suggest that the corrosion rate of Mg alloy in different media varied significantly. In general, lower corrosion rates were observed for the samples tested in organic-containing solutions such as DMEM and BCS. Moreover, the organic-containing synthetic and natural biological media showed a similar value. The results are consistent with the hydrogen evolution results obtained from the

immersion tests.

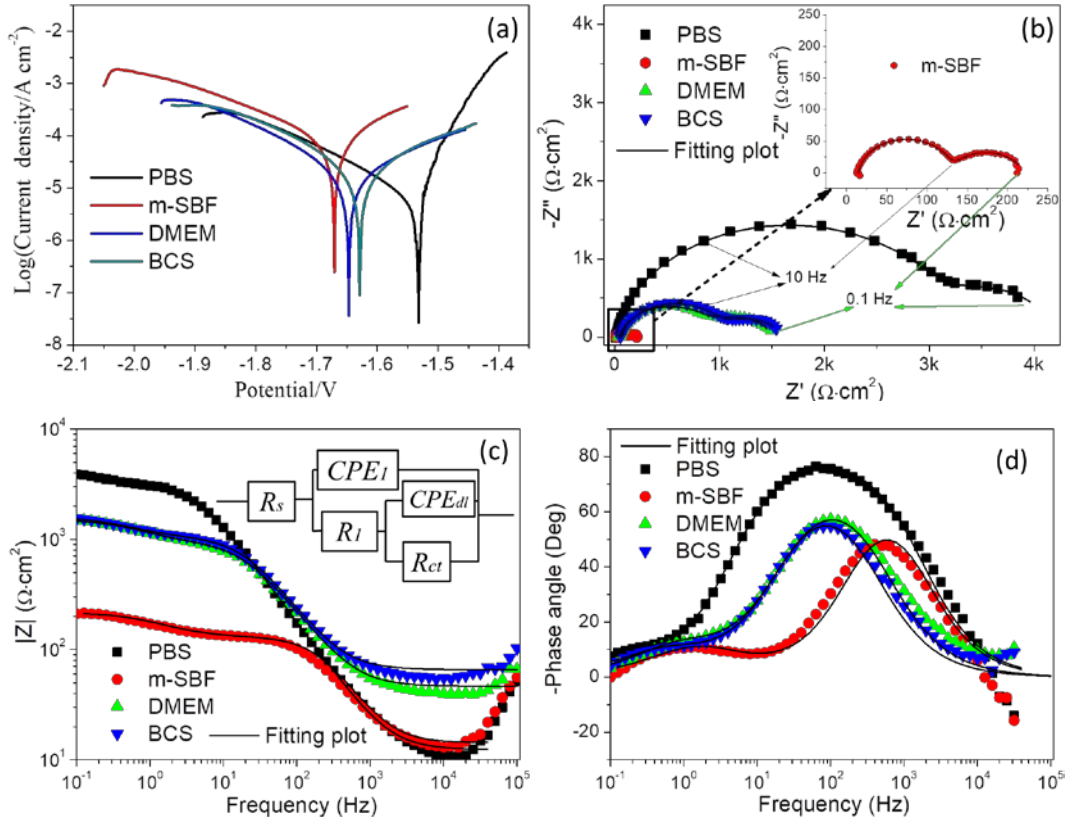


Fig. 3 (a) Potentiodynamic polarization (PDP) curves of the Mg-1Zn alloy after 0.5 h immersion in PBS, m-SBF, DMEM and BCS at 37 ± 1 °C; (b) Nyquist plots of the electrochemical impedance spectra (EIS) of the samples; (c)(d) Bode plots of EIS; Inset: equivalent circuit.

Table 2 EIS and PDP fitting results for samples tested in PBS, m-SBF, DMEM and BCS solution after 0.5 h immersion tests at 37 ± 1 °C.

Simplex	R_s $\Omega \cdot \text{cm}^2$	Q_{1-Y_0} (10^{-5} $\Omega^{-1} \cdot \text{cm}^2 \cdot \text{s}^n$)	Q_{1-n}	C_1 $\mu\text{F} \cdot \text{cm}^2$	R_l $\Omega \cdot \text{cm}^2$	Q_{dl-Y_0} (10^{-4} $\Omega^{-1} \cdot \text{cm}^2 \cdot \text{s}^n$)	Q_{dl-n}	R_{ct} $\Omega \cdot \text{cm}^2$	C_{dl} $\mu\text{F} \cdot \text{cm}^2$	E_{corr} V	i_{corr} $\mu\text{A} \cdot \text{cm}^{-2}$
In PBS	12±3	1.58±0.32	0.91±0.02	11.8	3319±133	11.83±1.44	1	845±43	1183	-1.53±0.07	4±1
In m-SBF	14±4	1.47±0.34	0.93±0.03	9.1	118±12	29.53±2.98	0.81±0.01	85±8	2135	-1.67±0.09	267±14
In DMEM	46±7	1.49±0.61	0.89±0.01	8.8	926±89	6.07±0.73	0.81±0.01	539±27	467	-1.65±0.11	11±3
In BCS	65±9	1.34±0.11	0.9±0.02	8.3	1000±187	8.64±0.72	0.79±0.02	544±54	707	-1.63±0.03	12±2

3.3 Fourier transformed infrared (FTIR) spectra and X-ray photoelectron spectroscopy (XPS) analysis

Fig. 4 shows the Fourier transformed infrared (FTIR) spectra of the Mg-1Zn alloy after 48 h of immersion in DW, PBS, m-SBF, DMEM and BCS. The adsorption bands at 3470 cm^{-1} , 1650 cm^{-1} and

550 cm^{-1} , corresponding to H_2O and/or OH^- vibrations, suggested the existence of hydrated species in the surface film [46,47]. The presence of stronger peaks at around 1030 cm^{-1} suggests the presence of phosphate products PO_4^{3-} on the surface of samples immersed in PBS and m-SBF, while not observed in DW [46,48]. The band from 1500 cm^{-1} to 1350 cm^{-1} refers to the bending and stretching vibrations of CO_3^{2-} ions [46,49]. Therefore, it can be concluded that the corrosion products on the Mg alloy surface contain carbonate compounds in all the solutions. The CO_3^{2-} ions found in DW might be attributed to the reaction of CO_2 from the air with superficial $\text{Mg}(\text{OH})_2$ during sample preparation after corrosion testing. The band near 1650 cm^{-1} can be ascribed to amide I of organic molecules [50]. The band at 1545 cm^{-1} could be ascribed to amide II, which was only observed for the samples immersed in DMEM and BCS. The above results indicate adsorption of organic components on the surface of the Mg-1Zn alloy when immersed in organic-containing biological media.

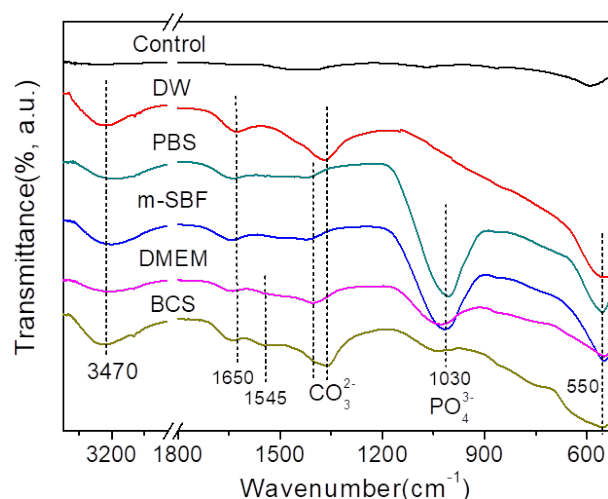


Fig. 4 FTIR spectra of the Mg-1Zn alloy after 48 h immersion in DW, PBS, m-SBF, DMEM and BCS.

To further investigate the adsorption of organic components on the surface of the Mg alloy, X-ray photoelectron spectroscopy (XPS) analysis was performed, and the results are shown in Fig. 5. The whole range of the binding energy survey of the XPS spectra are shown in Fig. 5a, indicating the

existence of carbon (C), oxygen (O), magnesium (Mg), nitrogen (N) and phosphorus (P) elements. N was not detectable for sample in DW, but it showed high intensity in DMEM and BCS (Fig. 5b). As shown in Fig 5c, d, e and f, N-1 (C-N) and N-2 (NH₂) bonds were observed at about 399.6 and 400.6 eV on the samples after immersion in DMEM and BCS. The intensity of C-1 (C=O/C=N), C-2 (C-O) and C-3 (C-C, C=C and C-H) at about 284.6, 285.9 and 287.8 eV were measured in DMEM, BCS and DW (Fig. 4g), which probably related to the C-O and CO₃²⁻ ions [46,51]. The high intensity of -COOH at about 290.4 eV (Fig. 5e and f) for the samples immersed in DMEM and BCS manifested that amino acids or glucose also might be adsorbed on the surface of the Mg alloy [52]. Fig. 5h shows the existence of Mg(OH)₂ after immersion in all solutions. The result suggests that the chemical composition of the surface corrosion layer was related to the composition of the solutions, and the deposition/adsorption of a mixture of organic and inorganic compounds on the surface, which is consistent with the results of FTIR and other studies [53,54].

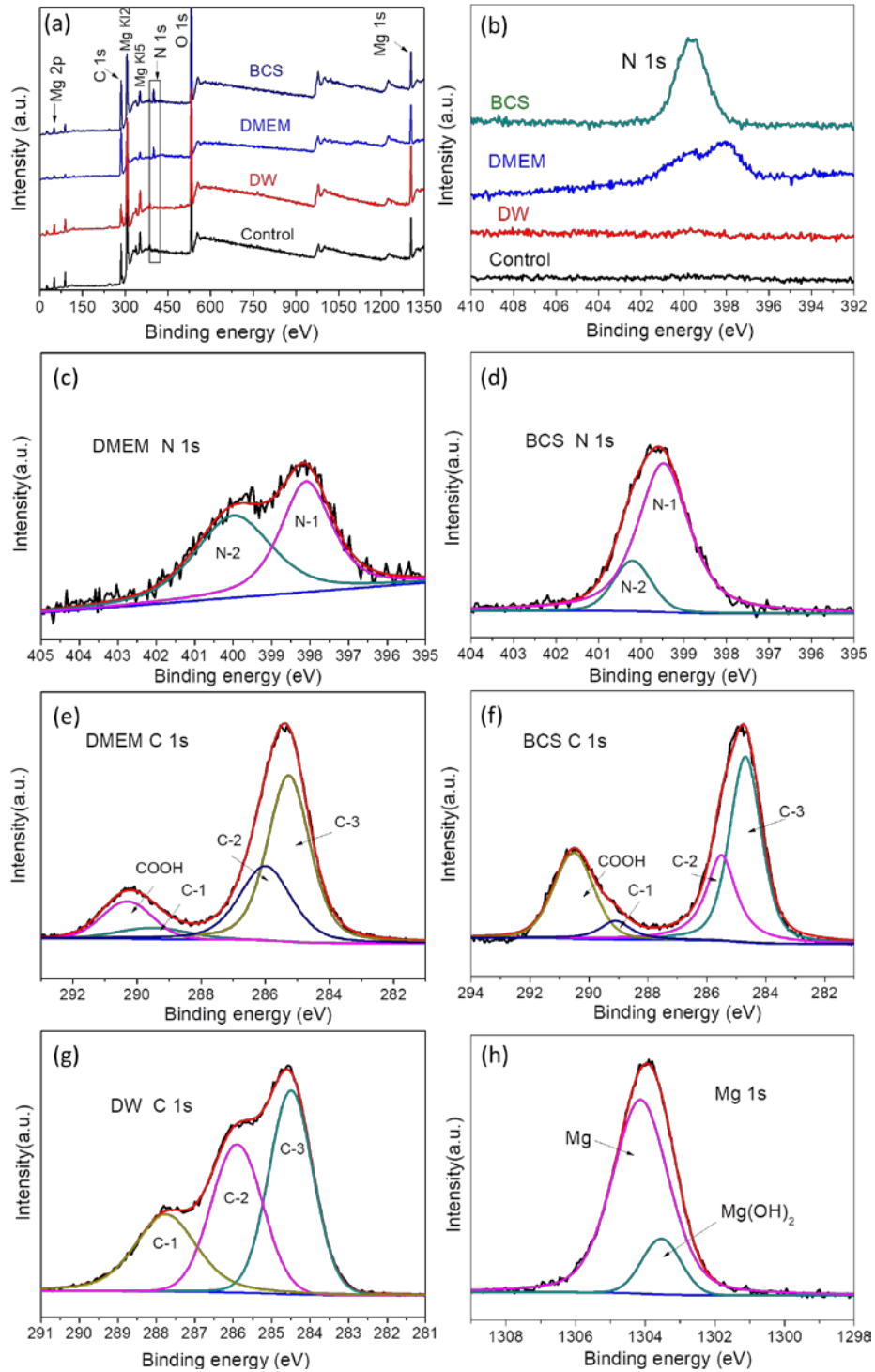


Fig. 5 XPS analysis of the Mg-1Zn alloy after 48 h immersion in control, DW, DMEM and BCS: (a) entire range of the binding energy survey; (b) N 1s spectra for the samples in control, DW, DMEM and BCS; representative N 1s spectra for the samples after 48 h immersion in (c) DMEM and (d) BCS; representative C 1s spectra for the samples immersion in (e) DMEM and (f) BCS; C 1s (g) spectra for the samples in DW and Mg 1s (h) for all samples.

3.4 Surface morphologies and EDS analysis after immersion tests

In order to investigate the degradation behaviour of the Mg-1Zn alloy in different solutions, the surface morphologies and EDS analysis of samples after 48 h of immersion with or without corrosion products are shown in Fig. 6. The main elements of the corrosion product were composed of O, Mg, P, N and Ca. EDS analysis shows that N was detected in DMEM and BCS in a small amount, while barely in PBS and m-SBF. The content of Ca was highest in m-SBF comparing with other solutions, but not in PBS. The Ca-P deposited layer generally could improve the corrosion resistance of Mg alloy in physiological solution [46]. The SEM morphologies of the surface show more homogenous corrosion layer and uniform dissolution of Mg alloy in DMEM and BCS, compared to that in PBS and m-SBF. The surface of the samples tested in PBS contains cluster-like precipitating products, which were insoluble salts owing to the high concentration of phosphate, an increasing Mg^{2+} concentration and thus a higher pH with the immersion time, as reported in previous work [21].

After removing the corrosion products, localized corrosion could be distinctly identified for the samples exposed to PBS and m-SBF under the topographical mode of SEM. While for samples exposed to DMEM and BCS, the surface are still relatively uniformly attached. The depth or area of corrosion sites for samples in m-SBF is larger than that of samples in BCS. The result manifested that the inorganic media (PBS and m-SBF) affect the chemical composition of surface corrosion layer and lead to a serious localized corrosion, while the cell culture medium (DMEM) and the natural biological media resulted in a more homogeneous degradation and lower corrosion rate for the biomedical Mg alloy.

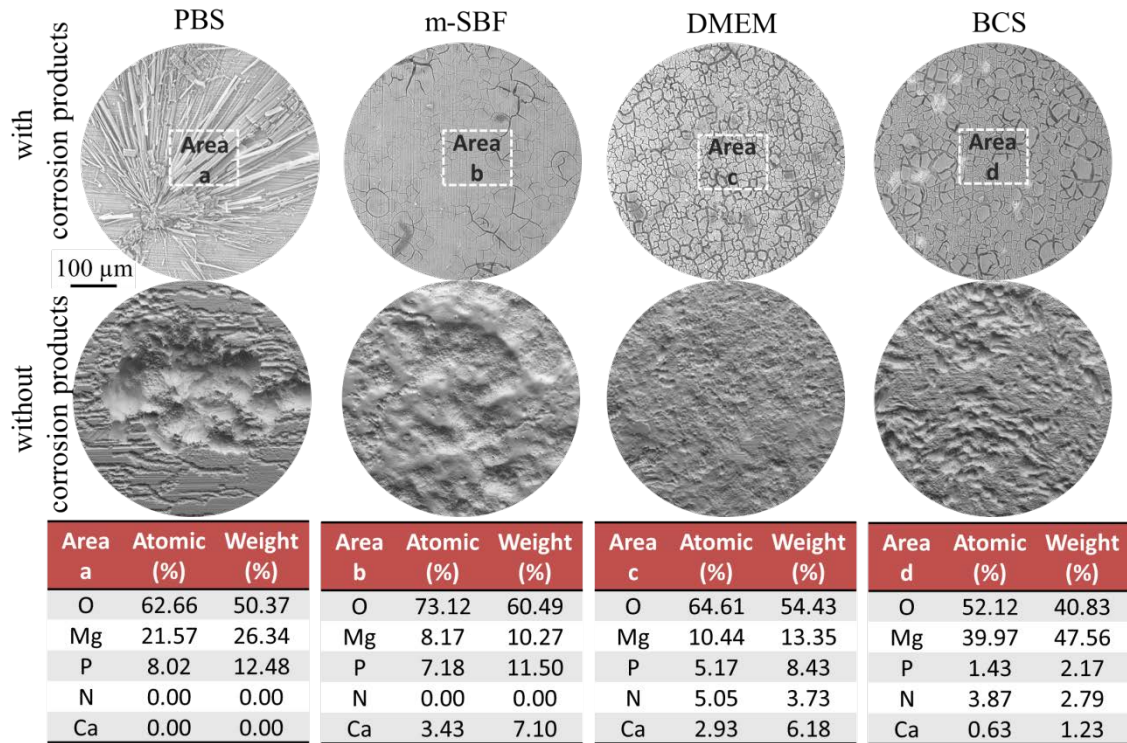


Fig. 6 The surface morphologies and EDS analysis of the Mg-1Zn alloy after 48 h of immersion in m-SBF, PBS, DMEM and BCS with or without corrosion products (Backscattered electron (BSE) full and topographical mode).

3.5 Slow strain rate tensile testing combined with electrochemical analysis

Fig. 7 shows the engineering stress-strain/time curves of the Mg-1Zn alloy at a strain rate of $1 \times 10^{-6} \text{ s}^{-1}$ tested in air, DW, PBS, m-SBF, DMEM and BCS. The mechanical properties of all the slow strain rate tensile (SSRT) tests results and the corresponding stress corrosion cracking (SCC) susceptibility indices (I_{sc}) calculated from ultimate tensile strength (UTS) and elongation to failure (ϵ) are listed in Table 3. The reduction of area (R_A) of all samples is 24.81 ± 5.44 , 6.84 ± 2.32 , 5.70 ± 1.07 , 7.02 ± 2.32 , 11.97 ± 2.89 and 14.03 ± 3.17 % corresponding to air, DW, PBS, m-SBF, DMEM and BCS, respectively. It is in the following order: air > BCS > DMEM > m-SBF > DW > PBS.

For the sample tested in DW, a significant loss in strength and ductility was observed in the SSRT tests, which indicate the SCC susceptibility for Mg alloys in water. The samples tested in PBS

exhibited a significantly higher $I_{sc}(\epsilon)$ of 0.62 and $I_{sc}(UTS)$ of 0.21, as compared to the other solutions. The mechanical properties of the samples tested in PBS suffered from a significant loss in ductility and strength. Comparing to the tests in air, the elongation to failure dropped from 17.91 ± 2.21 % to 6.72 ± 1.77 %, and the UTS and YS dropped from 285.00 ± 6.11 , 233.47 ± 11.21 MPa to 225.76 ± 9.88 , 161.61 ± 18.31 MPa, respectively. When inorganic or organic components were added into DW, such as DMEM, a further increase in elongation to failure than in DW was detected. A low SCC susceptibility index ($I_{sc}(UTS)$: 0.17, $I_{sc}(\epsilon)$: 0.34) for the sample tested in BCS was observed. The sample tested in BCS possessed adequate mechanical strength (YS: 190.59 ± 7.05 MPa, UTS: 237.20 ± 2.94 MPa) and elongation to failure (12.27 ± 1.89 %). Its ductility is almost twice larger than those tested in DW, which could ensure mechanical integrity and effectively avoid a sudden fracture failure. This result suggested that the synthetic cell culture and natural biological media showed the lowest stress corrosion cracking susceptibility for Mg-1Zn alloy, as compared to the solutions only containing inorganic ions.

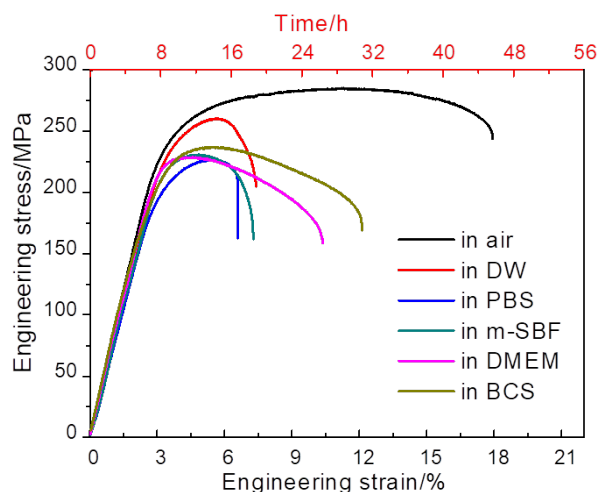


Fig. 7 Engineering stress-strain/time plots of Mg alloy at $1 \times 10^{-6} \text{ s}^{-1}$ strain rate in air, DW, PBS, m-SBF, DMEM and BCS.

Table 3 Summary of the slow strain rate tensile (SSRT) testing results and the stress corrosion cracking susceptibility indices (I_{sc}) of the samples tested in air, DW, PBS, m-SBF, DMEM and BCS.

Samples	UTS (MPa)	YS (MPa)	ϵ (%)	R_A (%)	I_{sc} (UTS)	I_{sc} (ϵ)
In air	285.00±6.11	233.47±11.21	17.91±2.21	24.81±5.44		
In DW	260.08±9.32	211.36±19.88	7.56±2.78	6.84±2.32	0.087	0.58
In PBS	225.76±9.88	161.61±18.31	6.72±1.77	5.70±1.07	0.21	0.62
In m-SBF	230.51±5.42	183.90±8.24	7.37±1.05	7.02±2.32	0.19	0.59
In DMEM	228.56±8.08	211.07±13.97	10.39±2.96	10.97±2.89	0.20	0.42
In BCS	237.20±2.94	190.59±7.05	12.27±1.89	12.03±3.17	0.17	0.31

The evolution of the open circuit potential (OCP) for the SSRT samples strained or unstrained in PBS, m-SBF, DMEM and BCS are shown in Fig. 8. The OCP evolution could refer to the activation or passivation of a sample, where a more positive OCP value represents a less reactive surface [41,55]. The plots of OCP could be divided into three stages according to the OCP fluctuation as a function of time, as observed for the samples tested in m-SBF, DMEM and BCS, however only two stages could be observed for the samples in PBS.

The breakage or dissolution of natural oxide film of Mg alloy could correspond to the change of OCP value during the initial stage (I) of the SSRT tests for the all samples, as shown in Fig. 8. The low fluctuation of OCP value for the samples strained or unstrained in PBS was observed during SSRT tests (Fig. 8a). The surface corrosion products formed in PBS might hardly be affected by the deformation strain of the Mg alloy. The OCP of the strained or unstrained samples in m-SBF, DMEM and BCS increased in stage two (II) (Fig. 8b, c and d), suggesting that the formation and deposition of corrosion products increased the corrosion resistance. For the unstrained samples in stage three (III, almost over the elastic-deformation period), the OCP shifted to positive level for the samples tested in m-SBF, or kept stable or fluctuation in DMEM and BCS. It inferred that the degradation rate reach a dynamic steady state, owing to the limited protective ability of passive film composed of inorganic and organic components. However, the OCP value of the strained samples tested in m-SBF increase slowly

comparing to that of the unstrained samples in stage three (III), even decreased in stage three for samples strained in DMEM and BCS. It might be related to plastic deformation would affect the corrosion behaviour of Mg alloy in m-SBF, DMEM and BCS. Finally, the fracture of the strained samples resulted in a sharply change of the OCP. It can be concluded that OCP changes in the unstrained condition was only related with the formation or breakdown of the surface corrosion product layer; OCP changes in strained condition was not only affected by the surface change due to static corrosion process, also affected by the mechanical breakdown and the rehabilitation process of corrosion product film in the plastic deformation region.

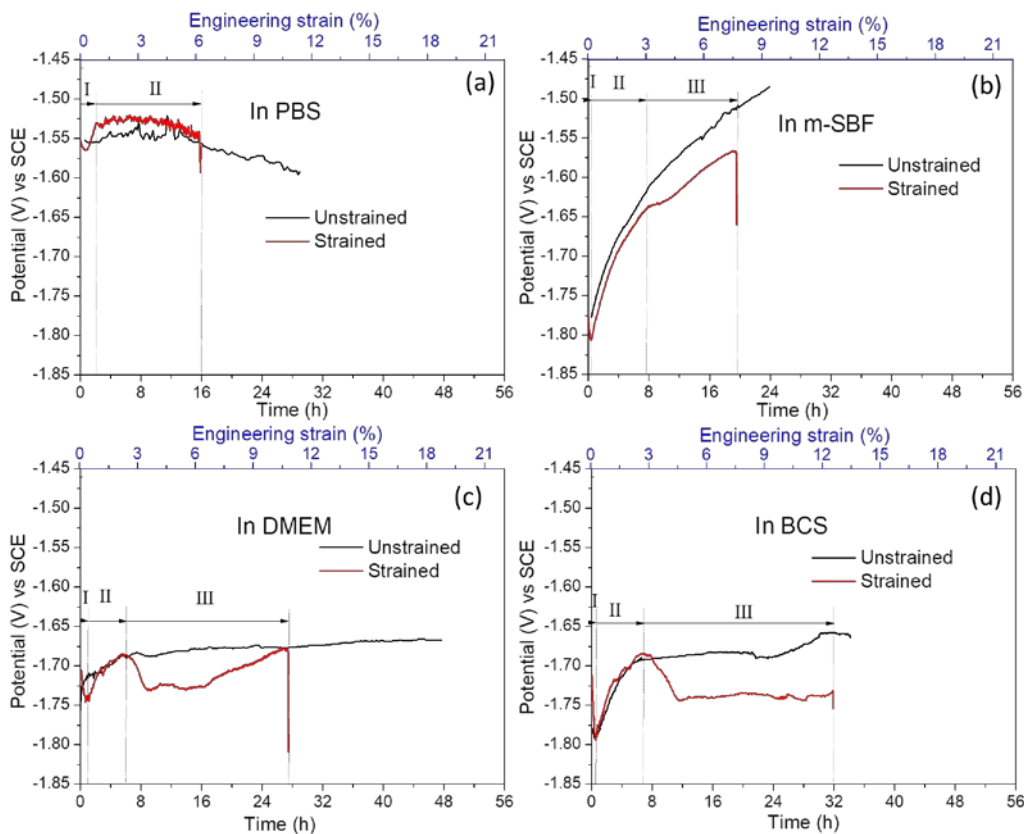


Fig. 8 The open circuit potential (OCP) evolution of the SSRT samples under strain or unstrained in (a) PBS, (b) m-SBF, (c) DMEM and (d) BCS as a function of time and engineering strain.

3.6 Fractographs and micro-cracks features

In order to analyse the fracture features of the samples after slow strain rate tensile (SSRT) tests,

SEM fractographs and EDS were studied and results are shown in Fig. 9. The overall fracture and higher magnification fractographs (Fig. 9 a1, a2 and a3) of the samples tested in air revealed a homogenous and fibrous fracture, with the presence of dimples and crack propagation direction at 45 °, demonstrating ductile failure occurred by mechanical overloading. The overall fracture surface of the SSRT samples measured in all solutions had two distinct regions: a stress corrosion cracking (SCC) region and a mechanical failure region (the yellow dotted line area). High magnification image of the SCC region showed a cleavage and a macroscopically brittle fracture, compared with that of the mechanical failure region, running from the circumference towards the centre of the samples. The SCC region of low alloyed and extruded Mg-1Zn alloy was related to the transgranular stress corrosion cracking (TGSCC), usually involving hydrogen embrittlement (HE) [7,12]. The fracture area for all samples in different solutions shown in Fig. 9 can infer that: $PBS \approx DW \approx m\text{-SBF} > DMEM > BCS > \text{air}$, which is consistent with the reduction in area (R_A) listed in Table 3, indicating a better ductility for the samples in DMEM and BCS solutions.

Moreover, the surface appearance of the fractured surface showed pitting acting as an initiation site for the stress corrosion cracking, and the micro-crack propagation direction was perpendicular to the tensile direction for the samples tested in DW, m-SBF, DMEM and BCS. When the micro-cracks initiating from the corrosion pits were developed into critical SCC cracks, the mechanical overloading happened at the final stage of the SSRT samples. A noticeable pitting and larger cleavage area was observed on the samples in PBS (Fig. 9c3). The red circle in Fig. 9e3 and the EDS mapping analysis in Fig. 9f3 showed the presence of C and N in the corrosion products, which is in consistence with the XPS results, representing the adsorption of organic component in the surface corrosion layer of Mg alloy. Although the Mg-1Zn alloy tested in different media exhibited a similar SCC failure features, i.

e., hydrogen embrittlement and mechanical overload failure zone, the former two exhibited different proportions in the fracture area of the SSRT samples.

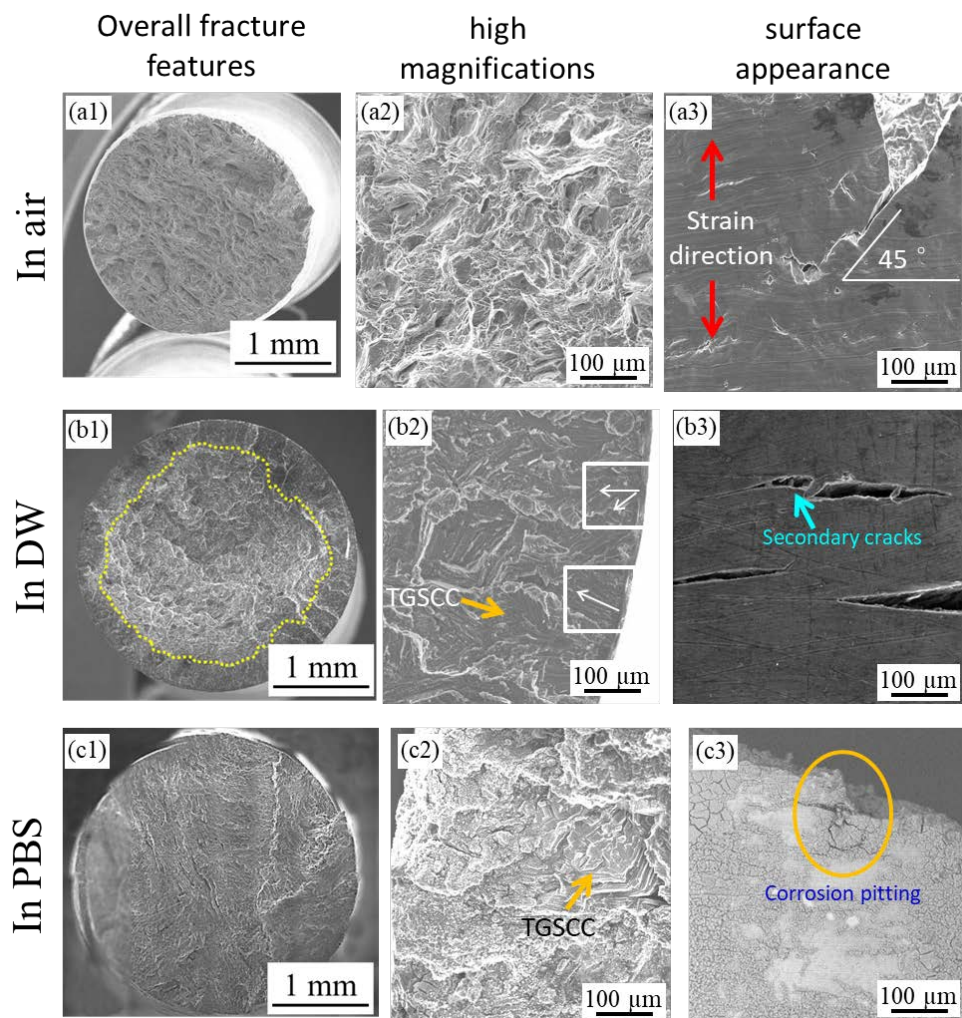
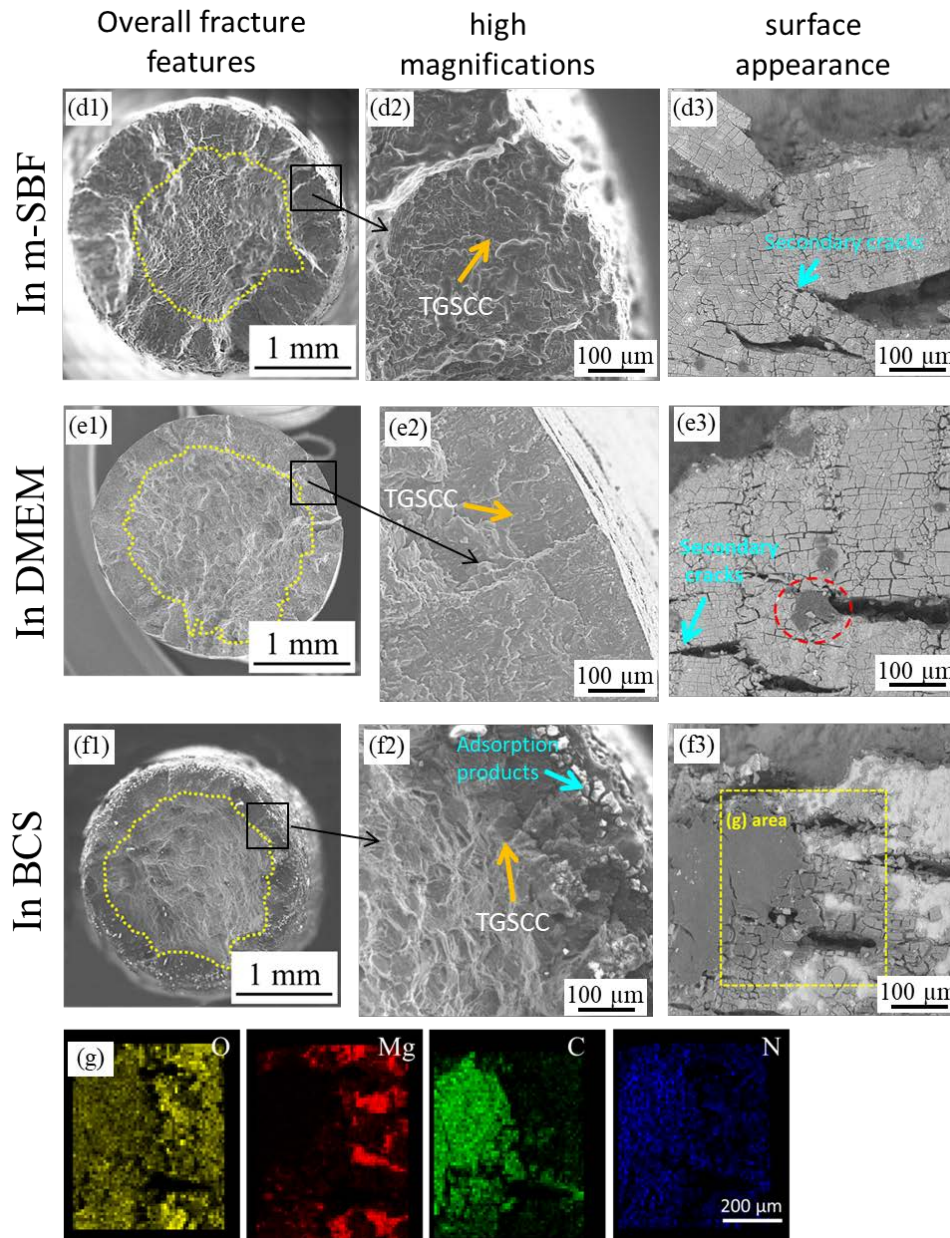


Fig. 9 The overall, higher magnification and surface appearance of the fracture features of the Mg-1Zn alloy tested in air (a1, a2, a3), in DW (b1, b2, b3) and in PBS (c1, c2, c3).



Continued Fig. 9 The overall, higher magnification and surface appearance of the fracture features of the Mg-1Zn alloy tested in m-SBF (d1, d2, d3), in DMEM (e1, e2, e3) and in BCS (f1, f2, f3) combined with the (g) area EDS mapping analysis.

In order to investigate the propagation of micro-cracks during SSRT tests in typical inorganic or natural media, the SEM and EDS of cross sections in m-SBF and BCS were measured and shown in Fig. 10a-c. Both the SSRT samples tested in solutions exhibited narrow micro-cracks perpendicular to the strain direction. The branches and main micro-cracks indicated the trans-granular cracking or preferential anodic dissolution [55]. However, the main micro-cracks were filled with corrosion

product for the sample tested in BCS, as shown in Fig. 10b. EDS of the corrosion products within the cracks (Fig. 10c) suggested that O, Mg and N signal was detected. However, the samples tested in m-SBF were not observed. The results confirmed that organic components or corrosion products were adsorbed into the crack tunnels for the samples tested in BCS.

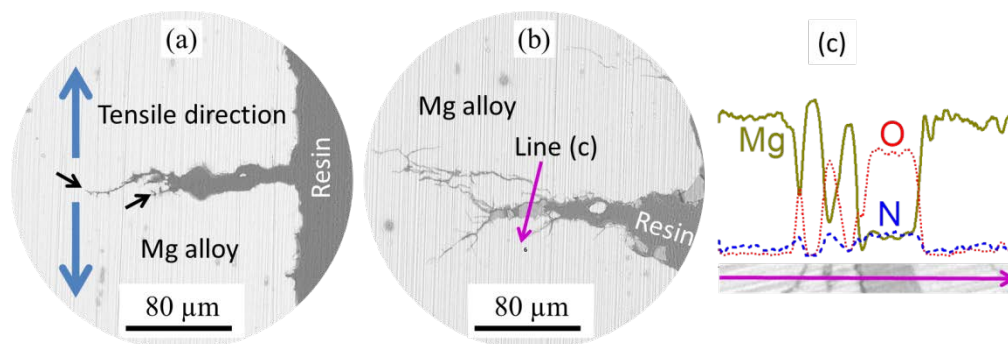
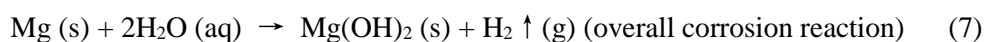
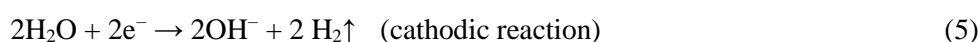


Fig. 10 The cross section SEM features of the slow strain rate tensile (SSRT) samples tested in (a) m-SBF and (b) BCS with the (c) EDS analysis of micro-cracking.

4 Discussion

4.1 Degradation behaviour of Mg in synthetic or natural media

The corrosion resistance of the Mg-1Zn alloy, as indicated by immersion tests (Fig. 2) and electrochemical measurements (Fig. 3), is in the following orders: DW > PBS > BCS > DMEM > m-SBF. For the samples tested in distilled water (DW), water could induce the corrosion reaction of Mg alloy owing to its low potential (-2.73 V vs. SHE) [1]. The main degradation reaction of Mg in physiological solutions can be described as [56-58];



In general, water can also induce a conversion of the surface oxide into $\text{Mg}(\text{OH})_2$ (as detected in FTIR and XPS, as shown in Fig. 4 and Fig. 5h), which could deposit on the surface of Mg alloy and acted as a passive film [44]. However, plasma and other media used in this work as listed Table 1 are chloride ions (Cl^-) containing aqueous solution, which can cause the dissolution of $\text{Mg}(\text{OH})_2$, leading to an accelerated corrosion of Mg alloy [59,60]. It leads to a higher corrosion rate of samples tested in PBS, m-SBF, DMEM and BCS than that in DW.

As an inorganic salt simulated media, m-SBF showed the highest corrosion rate, while PBS possessed the highest electrochemical impedance and corrosion resistance in this work. The chemical composition of m-SBF is similar to plasma, but with HEPES buffering reagent and a low concentration of HCO_3^- as shown in Table 1. The presence of Mg^{2+} , Ca^{2+} , HCO_3^- and HPO_4^{2-} ions in m-SBF could facilitate the formation of insoluble salts (Ca-P, (Mg, Ca)- CO_3 , Ca/Mg- PO_4), as shown in Fig. 4, Fig. 5 and Fig. 6) on the surface of Mg alloy. These corrosion products would improve the corrosion resistance as evidenced by the decrease of hydrogen gas evolution with immersion time (Fig. 2) [31,61]. However, as reported by previous works, HEPES would increase the dissolution rate of Mg alloy, compared to other solutions buffered with HCO_3^- ($44.1 \text{ mmol}\cdot\text{L}^{-1}$) [20]. This phenomenon could be demonstrated by the high corrosion rate (in Fig. 2 and Fig. 3), as well as the surface morphologies and pitting/localized corrosion (in Fig. 6) for the Mg-1Zn alloy immersed in m-SBF.

PBS buffering with high concentration of HPO_4^{2-} ions ($11.5 \text{ mmol}\cdot\text{L}^{-1}$) could form a flocculent water-containing layer on the surface of Mg alloy, which was observed during the immersion tests and after drying under SEM (Fig. 6). It is a single cluster-like precipitating and insoluble salt product ($\text{Mg}\cdot\text{PO}_4$, Fig. 6), which acted as a physical shield layer to improve the corrosion resistance of Mg alloy, as confirmed by the EIS results (Fig. 3). This result is consistent with previous works [35,62,63].

However, the insoluble corrosion products could form a micro-galvanic corrosion with surrounding Mg, resulting into accelerated corrosion of the anodic Mg. Thus the serious localised corrosion of samples observed in PBS could be explained, as shown the large corrosion pit in Fig.6.

DMEM and BCS media, both are natural organic-containing solutions buffered with HCO_3^- , exhibited lower corrosion rate and higher impedance value, compared to the samples immersed in m-SBF, as shown in Fig. 2 and Fig.3. In the present study, N element or C=N signals were detected on the samples immersed in DMEM and BCS (Fig. 4, Fig. 5 and Fig. 6) by FTIR, XPS and EDS analysis. It indicates that the protein or organic components from the DMEM and BCS are adsorbed on the surface of Mg alloys. The spontaneously adsorbed proteins acting as a physical shielding layer on biomaterial's surface has been reported already [25,64]. Previous works also reported that proteins such as fetal bovine serum could chelate with Mg^{2+} , and the serum molecules significantly retarded the corrosion of Mg alloy [1,20]. Meanwhile, the homogeneous corrosion surface observed in DMEM (Fig. 6) suggests that the adsorption and affinity of natural organic components on the samples could significantly suppress localized corrosion showing a reduced depth of pit formation [65]. Our results agreed with others' works [26,61,66], suggesting that organic components might be one of critical reasons causing different corrosion rates and degradation mechanisms between *in vitro* and *in vivo*.

4.2 Stress corrosion cracking susceptibility

As a loaded implant device, Mg alloys inevitably suffer from stress-assisted corrosion or stress corrosion cracking (SCC) failure under physiological stress or deformation residual stress, as reported by many studies [29,41,67]. Although some works have been dedicated to investigate the SCC susceptibility (I_{SCC}) of biomedical Mg alloys, the mostly used test environments were the inorganic synthetic solutions, such as PBS, SBF and Hank's solution [21]. Media containing organic components

such as natural bovine calf serum (BCS) and DMEM, which are much similar to *in vivo* physiological environment, were rarely used to determine the stress corrosion characteristics of Mg alloys. Fig. 11 shows that I_{SCC} data is obtained from the present work and others' previous work tested in a simulated physiological environment. The lowest I_{SCC} indices are observed from the Mg-1Zn alloys in BCS compared to the extruded Mg alloys in others' environment, indicating low stress corrosion cracking susceptibility in natural biological media.

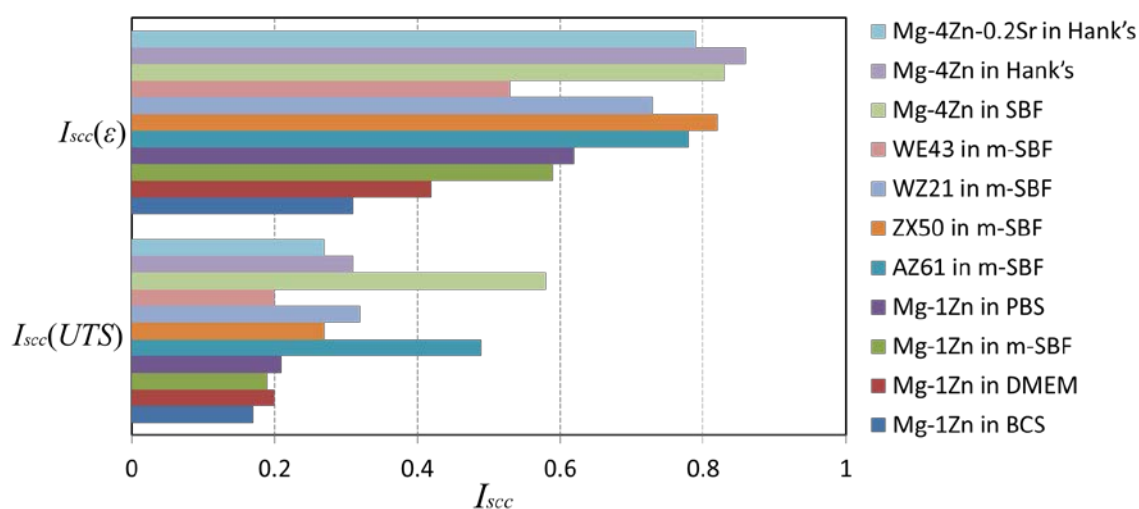


Fig. 11 I_{SCC} data of the Mg-1Zn alloy in PBS, m-SBF, DMEM and BCS compared to available data: Mg-4Zn-0.2Sr and Mg-4Zn in Hank's solution [68]; Mg-4Zn in SBF [9]; WE43, WZ21 and ZX50 in m-SBF [33]; AZ61 in m-SBF [55].

In this work, the SCC susceptibility of Mg-1Zn alloy was confirmed by hydrogen embrittlement and the propagation of micro-subcracks shown in SEM fractographs (Fig. 9 and Fig. 10). However, the loss of mechanical integrity of Mg alloy in different media was observed from the engineering stress-strain curves (Table 3), which was attributed to the various initiation pathways and propagation rate of SCC. The results showed that lower SCC susceptibility index was observed for slow strain rate tensile (SSRT) tests in DMEM and BCS, compared to PBS, m-SBF and distilled water (DW). The highest remaining ultimate tensile strength (UTS) and yield strength (YS) was measured in DW, which

might be attributed to the lower corrosion rate and absence of aggressive chloride ions in DW. However, the intrinsic susceptibility to SCC of Mg alloy resulted in a high loss of elongation to failure and premature fracture in DW [69]. It's worth noting that the elongation to failure (ϵ) for the samples tested in DMEM and BCS was still above 10 %, indicating that the ductility of the Mg-Zn alloy in those solutions was less influenced. The value of elongation to failure ϵ in BCS was nearly 2 times higher than in PBS and m-SBF, almost 68 % of the value obtained in air. The results revealed that the SCC susceptibility or sudden fracture features of Mg alloy in aqueous media were distinctly weakened in DMEM and BCS solutions.

Stress corrosion micro-cracks usually originated from pitting or localized corrosion, owing to the concentration of stress in the pits along with the difference in electrochemical potentials between those places and their adjacent region [12,70]. The severe pitting and localized corrosion, which are observed on the surface in PBS and m-SBF (Fig. 6 and Fig. 9c3), were likely to cause formation of micro-crack initiation sites in the early period of the SSRT tests. In contrast, the homogenous corrosion in DMEM and BCS could effectively avoid stress concentration at the beginning stage. Although the samples in PBS revealed a higher open circuit potential (OCP) and impedance (Fig. 8a and Fig. 3) compared with other solutions, the slight fluctuation of OCP during the SSRT manifested that the deformation of Mg alloy had little influence on the surface precipitating product. Considering the flocculent structure and outward growth of the film observed in immersion tests, it could be assumed that the surface products in PBS could not effectively prevent the initiation, even forming a micro-galvanic corrosion to accelerate the extension of micro-cracks in the matrix of the Mg alloy. These factors eventually resulted into the largest SCC indices for Mg alloys tested in PBS. However, for the samples in m-SBF, the evolution of OCP for the unstrained and the strained samples in Fig. 8b indicated that the

deformation might affect the protective ability of the surface deposition product. The high corrosion rate and unstable surface film finally lead to a high SCC susceptibility for the Mg-1Zn alloy in m-SBF.

The mechanical rupture of corrosion product layers triggered by deformation also resulted into the formation of stress concentration sites in Mg alloy, while organic components adsorbed then even form the complexes on the surface of Mg alloy would prevent the formation of micro-cracking initiation, due to their barrier effect [21,71,72]. Increasing the plastic deformation leads to a decrease of electrostatic repulsion between the metallic surface and the organic molecules, which promote the adsorption of negatively charged proteins [25]. Similar evolution of OCP at the beginning of the SSRT tests for the samples in DMEM and BCS manifested that the adsorption and chelation of organic components could sustain the protective ability of the surface corrosion layer. Although there is still controversy that protein chelating with the Mg-hydroxide film may facilitate localized corrosion when the chelation migrate away from the surface [29], the corrosion pits could also be sealed with the protein which acted as physical shield biofilm to modify the degradation behaviour [46]. The OCP fluctuation could be attributed to the competition between the mechanical rupture and the self-healing of the passive film [73]. Gao et al. [67] demonstrated that fibrotic capsule formed on the corrosion surfaces of HP Mg could significantly suppress the effects of stress-assisted degradation *in vivo*. The proteins adsorbed into the opened micro-cracks were hard to migrate and could even prevent the electrolyte exchange in the tunnel, then affecting the propagation of the micro-cracks (as shown in Fig. 9e3 and f3, Fig. 10b). In general, micro-cracks tend to propagate continually due to hydrogen embrittlement in aqueous solution, which normally leads to the continued film rupture in the cracking tip [12]. The fracture features (Fig.9) shows that all the SCC mechanism of Mg-1Zn alloy in media are related to the hydrogen embrittlement (HE), which involving hydrogen generated from the cathodic

reaction (equation (5)) [74,75]. In the present work, it was supposed that the hinder or consumption by the adsorption matter in the tunnel would go against the hydrogen evolution reaction in the micro-cracks by decreasing the matter exchange such as water, then affecting the source of hydrogen for causing HE and decreasing the propagation rate of SCC. For the samples tested in DMEM and BCS, the engineering stress-strain plots was shown that the tensile strength continuously decreased along with the increasing of elongation (Fig. 7), demonstrating that the SCC propagation was significantly suppressed. Specially, the presence of protein in solution may decrease the solution viscosity, then retarding the exchanging of the physiological compounds [61]. As a result, non-sudden fracture phenomenon in aqueous solution (elongation to failure $\varepsilon > 10\%$) during SSRT tests was observed in DMEM and BCS. It could be concluded that the SSRT samples tested in the DMEM or BCS showed a lower SCC susceptibility, compared to that in PBS and m-SBF. The stress corrosion cracking mechanism of the Mg-1Zn alloy in PBS, m-SBF, DMEM and BCS media could be elucidated by using the schematic diagrams, as shown in Fig. 12.

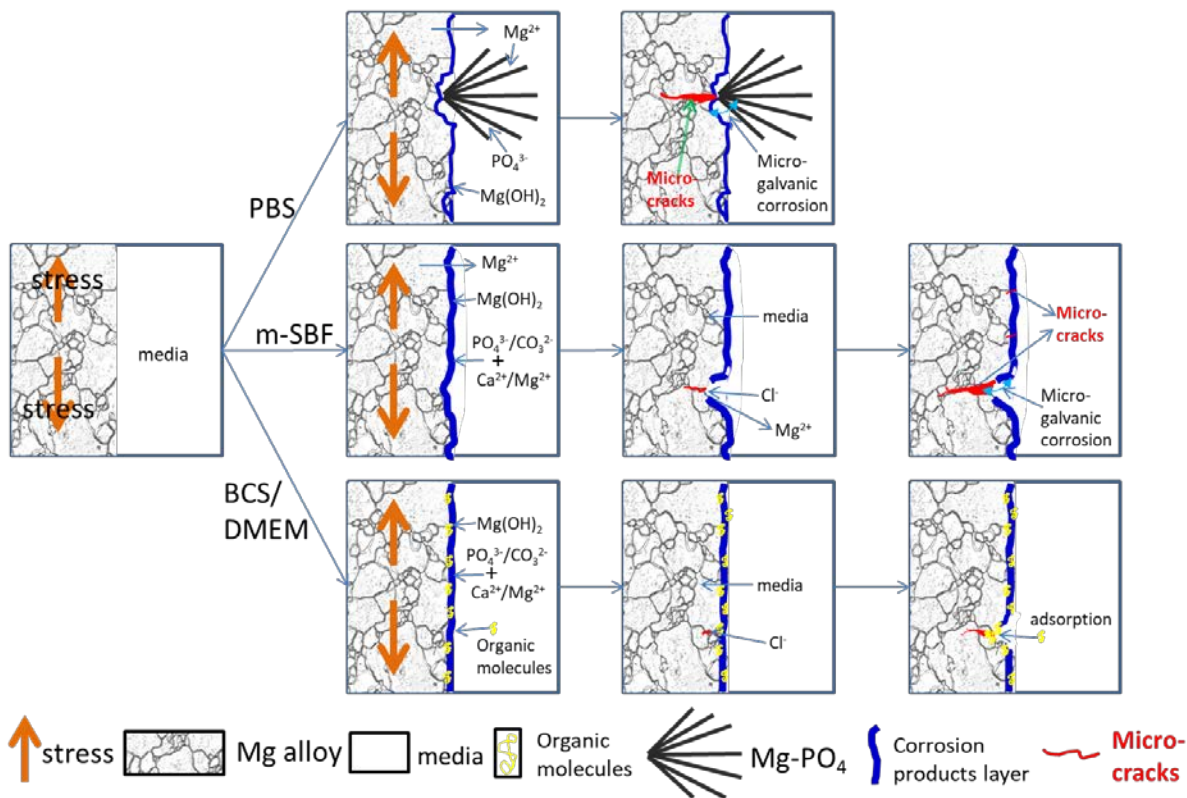


Fig. 12 Schematic diagrams of the stress corrosion cracking (SCC) behaviour of the Mg-1Zn alloy in PBS, m-SBF, DMEM and BCS media: in PBS, the micro-galvanic corrosion formed by the outward growth flocculent product accelerate the formation of stress concentration sites and hydrogen; in m-SBF, the pitting corrosion and break of surface film under deformation lead to a high SCC susceptibility; in DMEM and BCS, the homogeneous corrosion behaviour and adsorption of organic component into micro-tunnel retard the formation of stress initiation sites and electrolyte exchange then decreasing the propagation of SCC.

Our work suggests that organic components play an important role in the stress-assisted corrosion (degradation) process of biomedical Mg alloys. This work also indicates that simulated solutions that containing organic components such as serum, or natural biological media should be used for assessing the *in vitro* stress corrosion cracking of Mg alloys under sterile conditions in the future.

5 Conclusions

In this work, the stress corrosion cracking susceptibility of Mg-1Zn alloy using slow strain rate tensile (SSRT) tests in phosphate-buffered saline (PBS), modified simulated body fluid (m-SBF), Dulbecco's modified eagle medium (DMEM) and bovine calf serum (BCS) was investigated. The

surface corrosion products were characterized by the results of FTIR and XPS. The main conclusions are shown as following:

1) The corrosion rate of Mg alloy in all solutions was in the following order: m-SBF > DMEM > BCS > PBS > DW. The highest corrosion resistance of the surface corrosion products layer and serious pitting corrosion were both observed for the samples immersed in PBS.

2) The Mg-1Zn alloy exhibited improved resistance to corrosion and stress corrosion cracking in cell culture medium (DMEM) and BCS. It was attributed to the homogeneous corrosion, and the protection of the inorganic-organic hybrid corrosion product film, which retarded the initiation and propagation of micro-cracks during the SSRT testing.

3) The highest elongations to failure were obtained for samples in DMEM and BCS, which was still more than 50 % of that in air. The results indicated that Mg-1Zn alloy showed good toughness and ductile fracture failure in cell culture medium and natural animal-derived serum.

Acknowledge: This work was supported by Supported by National Key R&D Program of China (2017YFB0305100, 2017YFB0305104), the Science and Technology Planning Project of Guangdong Province No. 2017B090903005 and the Science and Technology Planning Project of Guangzhou No. 201704030045. XJW acknowledges the financial support from Jinan University (No. 88015139) and “Lan Huo” Research Funds (CXZJHZ201713). LXC acknowledges the financial support from China Postdoctoral Science Foundation (2018M643365) and the Basic and Applied Basic Research Fund of Guangdong Province (2019A1515110580).

Conflicts of Interest: The authors declare no conflict of interest.

Data availability: The raw/processed data required to reproduce these findings cannot be shared at this time as the data also forms part of an ongoing study.

References

- [1] Y.F. Zheng, X.N. Gu, F. Witte, Biodegradable metals, *Mater.Sci.Eng.*,R 77 (2014) 1-34.
- [2] W. Ding, Opportunities and challenges for the biodegradable Magnesium alloys as next-generation biomaterials, *Regen. Biomater.* 3 (2016) 79-86.
- [3] L. Tan, X. Yu, P. Wan, et al, Biodegradable materials for bone repairs:a review, *J.Mater.Sci.Technol.* 29 (2013) 503-513.
- [4] Y. Zhang, J. Xu, C.R. Ye, et al, Implant-derived Magnesium induces local neuronal production of CGRP to improve bone-fracture healing in rats, *Nat. Med.* 22 (2016) 1160-1169.
- [5] S.E. Harandi, R.S. Raman, Appropriate mechanochemical conditions for corrosion-fatigue testing of Magnesium alloys for temporary bioimplant applications, *JOM* 67 (2015) 1137-1142.
- [6] X.N. Gu, W.R. Zhou, Y.F. Zheng, et al, Corrosion fatigue behaviors of two biomedical Mg alloys - AZ91D and WE43 - In simulated body fluid, *Acta Biomater.* 6 (2010) 4605-4613.
- [7] S. Jafari, S.E. Harandi, R.S. Raman, A review of Stress-Corrosion cracking and corrosion fatigue of Magnesium alloys for biodegradable implant applications, *JOM* 67 (2015) 1143-1153.
- [8] J. Chen, M.R. Ai, J.Q. Wang, et al, Stress corrosion cracking behaviors of AZ91 Magnesium alloy in deicer solutions using constant load, *Mater.Sci.Eng.*,A 515 (2009) 79-84.
- [9] D.B. Prabhu, S. Dhamotharan, G. Sathishkumar, et al, Stress corrosion cracking of biodegradable Mg-4Zn alloy in simulated body fluid at different strain rates – A fractographic investigation, *Mater.Sci.Eng.*,A 730 (2018) 223 - 231.
- [10] G. Bombara, M. Cavallini, Stress corrosion cracking of bone implants, *Corros.Sci.* 17 (1977) 77-85.
- [11] Q. Chen, G.A. Thouas, Metallic implant biomaterials, *Mater.Sci.Eng.*,R 87 (2015) 1-57.
- [12] N. Winzer, A. Atrens, G. Song, et al, A critical review of the stress corrosion cracking (scc) of Magnesium alloys, *Adv.Eng.Mater.* 7 (2005) 659-693.
- [13] L. Chen, Y. Sheng, X. Wang, et al, Effect of the microstructure and distribution of the second phase on the stress corrosion cracking of biomedical Mg-Zn-Zr-xSr alloys, *Materials* 11 (2018) 1-17.
- [14] D.B. Prabhu, J. Nampoothiri, V. Elakkiya, et al, Elucidating the role of microstructural modification on stress corrosion cracking of biodegradable Mg4Zn alloy in simulated body fluid, *Mater.Sci.Eng.*,C 106 (2020) 110164.
- [15] Z. Shi, J. Hofstetter, F. Cao, et al, Corrosion and stress corrosion cracking of ultra-high-purity Mg5Zn, *Corros.Sci.* 93 (2015) 330–335.
- [16] M. Kappes, M. Iannuzzi, R.M. Carranza, Hydrogen embrittlement of Magnesium and Magnesium alloys: a review, *J.Electrochem.Soc.* 160 (2013) C C17-C168 .
- [17] N. Winzer, A. Atrens, W. Dietzel, et al, Fractography of stress corrosion cracking of Mg-Al alloys, *Metall.Mater.Trans.A* 39 (2008) 1 117-1157 .
- [18] F. Cao, Z. Shi, G.L. Song, et al, Stress corrosion cracking of several solution heat-treated Mg–X alloys, *Corros.Sci.* 96 (2015) 121-132.
- [19] M.B. Kannan, W. Dietzel, Pitting-induced Hydrogen embrittlement of Magnesium–aluminium alloy, *Mater.Des.* 42 (2012) 321 - 326.
- [20] A. Yamamoto, S. Hiromoto, Effect of inorganic salts, amino acids and proteins on the degradation of pure Magnesium in vitro, *Mater.Sci.Eng.*,C 29 (2009) 1559-1568.
- [21] J. Gonzalez, R.Q. Hou, E.P. Nidadavolu, et al, Magnesium degradation under physiological conditions– best practice, *Bioact mater* 3 (2018) 174 - 185.
- [22] D. Mei, S.V. Lamaka, J. Gonzalez, et al, The role of individual components of simulated body fluid on the corrosion behavior of commercially pure Mg, *Corros.Sci.* 147 (2019) 81 - 93.

- [23] Y. Koo, Y. Jang, Y. Yun, A study of long-term static load on degradation and mechanical integrity of Mg alloys-based biodegradable metals, *Mater.Sci.Eng.,B* 219 (2017) 45-54.
- [24] G.B. Hamu, D. Eliezer, L. Wagner, The relation between severe plastic deformation microstructure and corrosion behavior of AZ31 Magnesium alloy, *J.Alloys Compd.* 468 (2009) 222-229.
- [25] Z. Wang, Y. Yan, L. Qiao, Protein adsorption on implant metals with various deformed surfaces, *Colloids Surf.,B* 156 (2017) 62-70.
- [26] Y. Wang, S.L. Chu, V.L. Chao, et al, In vitro degradation behavior of M1A Magnesium alloy in protein-containing simulated body fluid, *Mater.Sci.Eng.,C* 31 (2011) 579-587.
- [27] S. Höhn, S. Virtanen, A.R. Boccaccini, Protein adsorption on Magnesium and its alloys: A review, *Appl.Surf.Sci.* 464 (2018) 212-219.
- [28] V. Wagener, A. Faltz, M.S. Killian, et al, Protein interactions with corroding metal surfaces: comparison of Mg and Fe, *Faraday Discuss.* 180 (2015) 347 - 360.
- [29] S.E. Harandi, P.C. Banerjee, C.D. Easton, et al, Influence of bovine serum albumin in Hanks' solution on the corrosion and stress corrosion cracking of a Magnesium alloy, *Mater.Sci.Eng.,C* 80 (2017) 335-345.
- [30] D. Xue, Y. Yun, Z. Tan, et al, In vivo and in vitro degradation behavior of Magnesium alloys as biomaterials, *J.Mater.Sci.Technol.* 28 (2012) 261 - 267.
- [31] L. Yang, E. Zhang, Biocorrosion behavior of Magnesium alloy in different simulated fluids for biomedical application, *Mater.Sci.Eng.,C* 29 (2009) 1691-1696.
- [32] S. Jafari, R.K. Raman, C.H. Davies, et al, Stress corrosion cracking and corrosion fatigue characterisation of MgZn1Ca0.3 (ZX10) in a simulated physiological environment, *J. Mech. Behav. Biomed.* 65 (2016) 634-643.
- [33] C. Lokesh, H. Joelle, P.J. Uggowitzer, In-vitro characterization of stress corrosion cracking of aluminium-free Magnesium alloys for temporary bio-implant applications, *Mater.Sci.Eng.,C* 42 (2014) 629-636.
- [34] A. Oyane, K. Onuma, A. Ito, et al, Formation and growth of clusters in conventional and new kinds of simulated body fluids, *J Biomed. Mater. Res. A* 64 (2003) 339-348.
- [35] Y. Xin, T. Hu, P.K. Chu, In vitro studies of biomedical Magnesium alloys in a simulated physiological environment: a review, *Acta Biomater.* 7 (2011) 1452-1459.
- [36] A. Oyane, H. Kim, T. Furuya, et al, Preparation and assessment of revised simulated body fluids, *J Biomed. Mater. Res. A* 65 (2003) 188 - 195.
- [37] L. Chen, Y. Bin, W. Zou, et al, The influence of Sr on the microstructure, degradation and stress corrosion cracking of the Mg alloys - ZK40xSr, *J. Mech. Behav. Biomed.* 66 (2016) 187-200.
- [38] J. Yang, C. Blawert, S.V. Lamaka, et al, Corrosion inhibition of pure Mg containing a high level of Iron impurity in pH neutral NaCl solution, *Corros.Sci.* 142 (2018) 222 - 237.
- [39] J. Li, Q. Jiang, H. Sun, et al, Effect of heat treatment on corrosion behavior of AZ63 Magnesium alloy in 3.5 wt.% Sodium chloride solution, *Corros.Sci.* 111 (2016) 288 - 301.
- [40] R. Hou, J. Victoria-hernandez, P. Jiang, et al, In vitro evaluation of the ZX11 Magnesium alloy as potential bone plate: Degradability and mechanical integrity, *Acta biomater.* 97 (2019) 608-622.
- [41] L.X. Chen, Y. Sheng, H.Y. Zhou, et al, Influence of a MAO + PLGA coating on biocorrosion and stress corrosion cracking behavior of a Magnesium alloy in a physiological environment, *Corros.Sci.* 148 (2019) 134-143.
- [42] Din, IOS 7539-7. Corrosion of metals and alloys - stress corrosion testing - part 7: method for slow strain rate testing. Berlin, Germany: Beuth Verlag GmbH, 2005.
- [43] D. Mei, S.V. Lamaka, X. Lu, et al, Selecting medium for corrosion testing of bioabsorbable Magnesium

- and other metals—a critical review, *Corros.Sci.* (2020) 108722.
- [44] P. Jiang, C. Blawert, N. Scharnagl, et al, Influence of water purity on the corrosion behavior of Mg0.5ZnX (X= Ca, Ge) alloys, *Corros.Sci.* (2019) 62-73.
- [45] C.L. Liu, Y.J. Wang, R.C. Zeng, et al, In vitro corrosion degradation behaviour of Mg–Ca alloy in the presence of albumin, *Corros.Sci.* 52 (2010) 3341-3347.
- [46] M. Ascencio, M. Pekguleryuz, S. Omanovic, An investigation of the corrosion mechanisms of WE43 Mg alloy in a modified simulated body fluid solution: The influence of immersion time, *Corros.Sci.* 87 (2014) 489-503.
- [47] Y. Wang, L.Y. Cui, R.C. Zeng, et al, In vitro degradation of pure Magnesium-The effects of glucose and/or amino acid, *Materials* 10 (2017) 725-741.
- [48] Y. Zhu, G. Wu, Y. Zhang, et al, Growth and characterization of Mg (OH) 2 film on Magnesium alloy AZ31, *Appl.Surf.Sci.* 257 (2011) 6129-6137.
- [49] M.I. Jamesh, G. Wu, Y. Zhao, et al, Effects of Zirconium and Oxygen plasma ion implantation on the corrosion behavior of ZK60 Mg alloy in simulated body fluids, *Corros.Sci.* 82 (2014) 7 - 26.
- [50] Y. Xin, K. Huo, H. Tao, et al, Influence of aggressive ions on the degradation behavior of biomedical Magnesium alloy in physiological environment, *Acta Biomater.* 4 (2008) 2008-2015.
- [51] L. Sai, J. Chen, Q. Chang, et al, Protein-derived Carbon nanodots with an ethylenediamine-modulated structure as sensitive fluorescent probes for Cu 2+ detection, *RSC Advances* 7 (2017) 11661-11668.
- [52] R. Zeng, X. Li, S. Li, et al, In vitro degradation of pure Mg in response to glucose, *Sci. Rep.* 5 (2015) 13026.
- [53] S. Zanna, C. Compère, P. Marcus, XPS characterisation of BSA adsorption on stainless steel, *Elsevier Science* (2006) 365-370..
- [54] B. Ahmed, H. Surat, C. Robert, et al, Locating the binding sites of Pb(II) ion with human and bovine serum albumins, *Plos One* 7 (2012) e36723.
- [55] K. Törne, A. Örnberg, J. Weissenrieder, Influence of strain on the corrosion of Magnesium alloys and Zinc in physiological environments, *Acta Biomater.* 48 (2017) 541-550.
- [56] R.G. Song, C. Blawert, W. Dietzel, et al, A study on stress corrosion cracking and Hydrogen embrittlement of AZ31 Magnesium alloy, *Mater.Sci.Eng.,A* 399 (2005) 308-317.
- [57] R.C. Zeng, L.Y. Cui, K. Jiang, et al, In vitro corrosion and cytocompatibility of a microarc oxidation coating and Poly(L-lactic acid) composite coating on Mg-1Li-1Ca alloy for orthopedic implants, *ACS Appl. Mater. Interfaces* 8 (2016) 10014-11002.
- [58] E.L. Silva, S.V. Lamaka, D. Mei, et al, The reduction of dissolved Oxygen during Magnesium corrosion, *ChemistryOpen* 7 (2018) 664 - 668.
- [59] Y. Chen, Z. Xu, C. Smith, et al, Recent advances on the development of Magnesium alloys for biodegradable implants, *Acta Biomater.* 10 (2014) 4561-4573.
- [60] N. Hara, Y. Kobayashi, D. Kagaya, et al, Formation and breakdown of surface films on Magnesium and its alloys in aqueous solutions, *Corros.Sci.* 49 (2007) 166 - 175.
- [61] R. Hou, N. Scharnagl, R. Willumeit-römer, et al, Different effects of single protein vs. protein mixtures on Magnesium degradation under cell culture conditions, *Acta Biomater.* 98 (2019) 256-268.
- [62] C. Schille, M. Braun, H.P. Wendel, et al, Corrosion of experimental Magnesium alloys in blood and PBS: A gravimetric and microscopic evaluation, *Mater.Sci.Eng.,B* 176 (2011) 1 180-1797 .
- [63] W. Mueller, M. Fernandez lorenzo de mele, M.L. Nascimento, et al, Degradation of Magnesium and its alloys: dependence on the composition of the synthetic biological media, *J Biomed. Mater. Res. A* 90 (2009) 487 - 495.

- [64] P. Satzer, F. Svec, G. Sekot, et al, Protein adsorption onto nanoparticles induces conformational changes: Particle size dependency, kinetics, and mechanisms, *Eng. Life Sci.* 16 (2016) 238-246.
- [65] I. Johnson, W. Jiang, H. Liu, The effects of serum proteins on Magnesium alloy degradation in vitro, *Sci. Rep.* 7 (2017) 14335.
- [66] X.N. Gu, Y.F. Zheng, L.J. Chen, Influence of artificial biological fluid composition on the biocorrosion of potential orthopedic Mg–Ca, AZ31, AZ91 alloys, *Biomed. Mater.* 4 (2009) 065011.
- [67] Y. Gao, L. Wang, L. Li, et al, Effect of stress on corrosion of high-purity Magnesium in vitro and in vivo, *Acta Biomater.* 83 (2019) 477 - 486.
- [68] Z. Yu, J. Chen, H. Yan, et al, Degradation, stress corrosion cracking behavior and cytocompatibility of high strain rate rolled Mg-Zn-Sr alloys, *Mater.Lett.* 260 (2020) 126920.
- [69] F. Cao, Z. Shi, G.L. Song, et al, Stress corrosion cracking of several hot-rolled binary Mg–X alloys, *Corros.Sci.* 98 (2015) 6-19.
- [70] Winzer, Atrens, Dietzel, et al, Characterisation of stress corrosion cracking (SCC) of Mg-Al alloys, *Mater.Sci.Eng.,A* 488 (2008) 339-351.
- [71] Z. Zhang, L. Wang, M. Zeng, et al, Biodegradation behavior of micro-arc oxidation coating on Magnesium alloy-from a protein perspective, *Bioact. Mater.*5 (2020) 398 - 409.
- [72] S. Höhn, S. Virtanen, A.R. Boccaccini, Protein adsorption on Magnesium and its alloys: A review, *Appl.Surf.Sci.* 464 (2019) 212 - 219.
- [73] E.M. Hernández, E.I. Franses, Adsorption and surface tension of fibrinogen at the air/water interface, *Colloids Surf.,A* 214 (2003) 249 - 262.
- [74] N. Winzer, A. Atrens, W. Dietzel, et al, Evaluation of the delayed hydride cracking mechanism for transgranular stress corrosion cracking of Magnesium alloys, *Mater.Sci.Eng.,A* 466 (2007) 18 - 31.
- [75] S.D. Wang, D.K. Xu, B.J. Wang, et al, Effect of solution treatment on stress corrosion cracking behavior of an as-forged Mg-Zn-Y-Zr alloy, *Sci Rep.* 6 (2016) 1-12.